








3D magnetic configuration of ferrimagnetic multilayers with competing interactions visualized by soft X-ray vector tomography

Javier Hermosa-Muñoz ^{1,2}, Aurelio Hierro-Rodríguez ^{1,2}✉, Andrea Sorrentino ³, José I. Martín ^{1,2}, Luis M. Alvarez-Prado^{1,2}, Stefan Rehbein⁴, Eva Pereiro ³, Carlos Quirós^{1,2}, María Vélez ^{1,2}✉ & Salvador Ferrer ³✉

Full control of magnetic properties in exchange coupled systems requires a good understanding of 3D magnetic configuration with lateral and in-depth resolution. Here we show results from a soft X-ray tomographic reconstruction which allow determining, solely from the experimental data, a detailed description of the vector magnetic configuration of a ferrimagnetic $\text{Gd}_{12}\text{Co}_{88}/\text{Nd}_{17}\text{Co}_{83}/\text{Gd}_{24}\text{Co}_{76}$ trilayer with engineered competing anisotropy, exchange and magneto-static interactions at different depths. The trilayer displays chevron patterns with a distorted closure structure. Near the top $\text{Gd}_{24}\text{Co}_{76}$ layer, local exchange springs with out-of-plane magnetization reversal, quasi-domains with ripple-like patterns and magnetic vortices and antivortices across the thickness are observed. The detailed analysis of the magnetic tomogram shows that the effective strength of the exchange spring at the NdCo/GdCo interface can be finely tuned by $\text{Gd}_x\text{Co}_{1-x}$ composition and anisotropy (determined by sample fabrication) and in-plane stripe orientation (adjustable), demonstrating the suitability of 3D magnetic visualization techniques in magnetic engineering research.

¹Depto. Física, Universidad de Oviedo, 33007 Oviedo, Spain. ²CINN (CSIC - Universidad de Oviedo), 33940 El Entrego, Spain. ³ALBA Synchrotron, 08290 Cerdanyola del Vallès, Spain. ⁴Helmholtz Zentrum Berlin für Materialien und Energie GmbH, 12489 Berlin, Germany. ✉email: hierroaurelio@uniovi.es; mvelez@uniovi.es; ferrer@cells.es

Advanced spintronic devices and magnetic recording media require control and characterization of multilayer magnetic systems in which the desired magnetic behaviour has to be precisely adjusted by properly tuning magnetic interactions such as exchange and magnetostatics^{1,2}. For example, ferrimagnetic materials, such as Gd-Co alloys^{3,4} with their adjustable magnetization, offer the possibility of controlling spin-wave modes⁵, spin-orbit torque, skyrmion nucleation, and fast domain wall motion^{6–9} and, even, of engineering magnetocaloric effects in multilayers¹⁰.

Exchange springs are very interesting features to tune the magnetic behavior of a system: when two exchange-coupled magnetic layers have very different magnetic anisotropy¹¹, they originate characteristic domain walls at the interfaces to accommodate the reversible rotation of the soft magnetic layer under an applied field, while the hard layer stays pinned in its original magnetic configuration. They are versatile magnetic systems since they can be easily tuned adjusting the individual layer thickness and interlayer coupling strength^{12–20}. For example, exchange springs have been widely explored in order to maximize the energy product $(BH)_{\max}$ for permanent magnet applications²¹. Exchange springs exist in ferrimagnetic multilayers both in materials with in-plane^{12,13} and out-of-plane^{14–17} magnetic anisotropy, or even crossed¹⁸ and chiral anisotropies¹⁹.

Most of the previous studies are based in measurements of hysteresis loops and the domain structures, which are instrumental for the understanding magnetization reversal, are inferred indirectly from comparisons with micromagnetic simulations¹⁸. Microscopy techniques such as Magnetic Force microscopy (MFM) can also be used to disentangle magnetization reversal at the nanoscale as has been recently reported in ferro/ferrimagnetic NiCoPt/TbFeCo but, again, with the support of micromagnetic simulations of the observed magnetic contrast²². Magneto-optical microscopy, which is a powerful technique for domain analysis in thin films, has also been used to separate the contribution of few nm thick individual layers in magnetic sandwiches²³. More detailed in-depth characterization of magnetization profiles of interfacial domain walls can be obtained by magnetic reflectometry with either neutron²⁰ or X-ray-based techniques^{12,24,25} but mainly in systems with homogeneous or periodic configuration.

Full control of global and local magnetic properties in exchange-coupled multilayers requires a good understanding of the 3D magnetic structures with appropriate lateral and in-depth resolutions. An initial approach based on element-specific Magnetic Transmission X-ray Microscopy (MTXM) allowed to identify different magnetization reversal processes across the thickness of GdCo/NdCo/NiFe multilayers^{26–28} and the physics of magnetic vortex imprinting in NiFe/CoPt nanostructures²⁹. More recently, the development of Transmission X-ray Vector Tomography and Laminography^{30,31} has allowed resolving magnetization vector fields in 3D and has opened a fully experimental approach to study complex magnetization textures. These methods exploit X-ray Magnetic Circular Dichroism and differently oriented projections of the sample to be able to reconstruct its inner magnetic configuration^{32,33}. It has also been extended to dynamics allowing for 4D mapping of the magnetization³⁴. MTXM has demonstrated to be excellent for revealing the nature of magnetic singularities, nontrivial magnetic topological textures, and complex magnetization configurations^{30,35–37}.

In the present article, we report the results of exploiting the capabilities of magnetic vector tomography to determine the magnetization of a complex magnetic trilayer engineered to have competing or favoring exchange/magnetostatic interactions at different depths. The detailed analysis of the remnant magnetic configuration reveals a 3D structure that combines stripe domains, exchange spring walls across the thickness, and

quasi-domains with ripple-like patterns. In-plane stripe domain orientation, adjustable through magnetic history, appears as the relevant parameter to control the strength of global interlayer coupling.

Results and discussion

Multilayer design. We have prepared an 80 nm Gd₁₂Co₈₈/80 nm Nd₁₇Co₈₃/80 nm Gd₂₄Co₇₆ multilayer designed to support an exchange spring at the top layer. Ferrimagnetic Gd_xCo_{100-x} alloys present a soft magnetic behaviour with in-plane uniaxial anisotropy, whereas the stoichiometry of the central Nd₁₇Co₈₃ layer corresponds to a ferromagnetic alloy with weak perpendicular anisotropy (see Fig. 1(a)). The purpose of the central layer, which had the largest anisotropy in the multilayer, is to create a pattern of stripe domains with alternating up-down magnetization orientation^{26,38} that can be used to control the configuration in the neighbouring Gd_xCo_{100-x} layers via interfacial exchange and magnetostatic interactions. Also, the stripe pattern provides an interesting possibility for external adjustment of the system after sample fabrication: stripe orientation can be rotated at will with large enough in-plane magnetic fields and becomes locked at low fields by the so-called rotatable anisotropy^{39,40}, which is an in-plane pseudouniaxial anisotropy of magnetostatic origin with easy axis along the direction of the stripes.

The magnetization of the ferrimagnetic Gd_xCo_{100-x} alloy is given by the sum of the contributions of Co and Gd atom sublattices¹². The magnetization vectors of each sublattice can be written as $\mathbf{M}(\text{Co}) = M(\text{Co})\mathbf{m}(\text{Co})$ and $\mathbf{M}(\text{Gd}) = M(\text{Gd})\mathbf{m}(\text{Gd})$, where $M(\text{Co})$ and $M(\text{Gd})$ are the magnetization magnitudes and $\mathbf{m}(\text{Co})$ and $\mathbf{m}(\text{Gd})$ are unit vectors. In these Gd_xCo_{100-x} alloys, Gd and Co moments are collinear and antiparallel, so that $\mathbf{m}(\text{Gd}) = -\mathbf{m}(\text{Co})$.

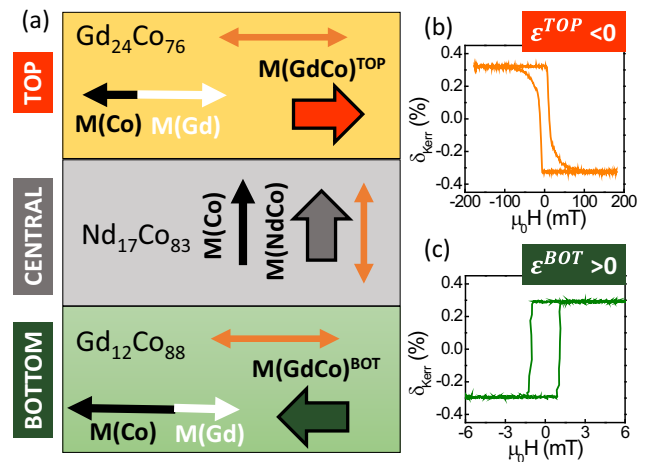


Fig. 1 Multilayer design for adjustable exchange spring. **a** Sketch of multilayer structure. Black/white thin arrows indicate magnetization of Co and Gd atom sublattices, $\mathbf{M}(\text{Co})$ and $\mathbf{M}(\text{Gd})$, respectively. Thick arrows indicate net magnetization $\mathbf{M}(\text{GdCo})$. Double orange arrows indicate anisotropy easy axis. **b** Room temperature Transverse MOKE hysteresis loop δ_K vs. field (with $\delta_K = \frac{\Delta R}{R}$ the fractional change in sample reflectance⁴¹) of 50 nm Gd₂₄Co₇₆ control sample, sensitive only to Co atom sublattice. Note the negative signal at saturation in a positive field, indicating the antiparallel alignment between $\mathbf{M}(\text{GdCo})^{\text{TOP}}$ and $\mathbf{m}(\text{Co})^{\text{TOP}}$, i.e. $\epsilon^{\text{TOP}} < 0$. **c** Room temperature MOKE hysteresis loop of 50 nm Gd₁₂Co₈₈ control sample with positive signal at positive saturation field, corresponding to parallel $\mathbf{M}(\text{GdCo})^{\text{BOT}}$ and $\mathbf{m}(\text{Co})^{\text{BOT}}$, i.e. $\epsilon^{\text{BOT}} > 0$. The sign of ϵ , which is opposite at Top/Bottom layers, will determine whether interfacial, exchange and magnetostatic interactions between NdCo and GdCo layers either cooperate or compete with each other. The exchange spring will appear at the surface with $\epsilon < 0$, as discussed in the text.

The net magnetization of the alloy $\mathbf{M}(\text{GdCo})$ is given by

$$\mathbf{M}(\text{GdCo}) = \mathbf{M}(\text{Co}) + \mathbf{M}(\text{Gd}) = (M(\text{Co}) - M(\text{Gd}))\mathbf{m}(\text{Co}) = \varepsilon\mathbf{m}(\text{Co}) \quad (1)$$

where $\varepsilon = M(\text{Co}) - M(\text{Gd})$ is a scalar factor that relates $\mathbf{M}(\text{GdCo})$ with $\mathbf{m}(\text{Co})$. The saturation magnetization of the alloy is $M_s(\text{GdCo}) = |M(\text{Co}) - M(\text{Gd})| = |\varepsilon|$. Depending on temperature and composition, ε may be either positive ($M(\text{Co}) > M(\text{Gd})$) or negative ($M(\text{Co}) < M(\text{Gd})$). In-plane magnetized $\text{Gd}_x\text{Co}_{100-x}/\text{Gd}_y\text{Co}_{100-y}$ exchange springs are usually designed by finely tuning the alloy composition so that ε has opposite signs at each layer¹².

Here, the composition of the bottom $\text{Gd}_{12}\text{Co}_{88}$ layer has been chosen so that its saturation magnetization $M_s(\text{GdCo})^{\text{BOT}}$ is large and ε^{BOT} is positive at room temperature. On the contrary, the top layer $\text{Gd}_{24}\text{Co}_{76}$ composition is selected so that its compensation temperature is slightly above room temperature which implies that $M_s(\text{GdCo})^{\text{TOP}}$ is small and ε^{TOP} is negative. The sign of ε was determined by Transverse Magneto-optical Kerr effect (MOKE) hysteresis loops (see Fig. 1(b, c))⁴¹, measured at room temperature with white light, on 50 nm thick $\text{Gd}_x\text{Co}_{100-x}$ control samples with the same composition as top/bottom layers in the trilayer. For incident light in the visible, MOKE is only sensitive to Co magnetic moments¹². Then, at positive applied fields, $\varepsilon^{\text{BOT}} > 0$ implies a positive MOKE signal and $\mathbf{m}(\text{Co})^{\text{BOT}}$ parallel to $\mathbf{M}(\text{GdCo})^{\text{BOT}}$ (see Fig. 1(c)). On the contrary, $\varepsilon^{\text{TOP}} < 0$ implies negative MOKE signal at positive applied fields since $\mathbf{m}(\text{Co})^{\text{TOP}}$ is antiparallel to $\mathbf{M}(\text{GdCo})^{\text{TOP}}$ (see Fig. 1(b)).

The magnetization configuration of GdCo layers will depend on three competing interactions across the sample thickness related with the magnetic parameters selected for each layer in these $\text{Gd}_{12}\text{Co}_{88}/\text{Nd}_{17}\text{Co}_{83}/\text{Gd}_{24}\text{Co}_{76}$ multilayers (see sketch in Fig. 1(a)). The first one is the exchange interaction at the interfaces, which in Rare Earth-Transition Metal alloys is dominated by $J(\text{Co} - \text{Co})$, the exchange between Co moments¹² and favours the parallel alignment of $\mathbf{m}(\text{Co})$ at the different layers. The second is the uniaxial anisotropy with out-of-plane easy axis at the central layer and in-plane easy axis at the outer layers. Finally, magnetostatic interactions will try to minimize magnetic charges (i.e. discontinuities in the magnetization), creating closure domains and favouring parallel alignment of $\mathbf{M}(\text{GdCo})$ and $\mathbf{M}(\text{NdCo})$ at the interfaces, which may either compete or cooperate with interfacial exchange depending on the sign of ε .

In summary, our multilayer design includes a laterally modulated domain structure (stripe domains) that can be adjusted with magnetic history, and competing exchange, anisotropy and magnetostatic interactions across the multilayer thickness. As described in what follows, vector tomography has allowed visualizing the complex domain structure demonstrating its capabilities in magnetic engineering research.

Soft X-ray MTXM and vector tomography. Figure 2 shows several MTXM images, measured at the Gd $M_{4,5}$ absorption edge with different angles of incidence so that they are sensitive to the different components of the magnetic moment $\mathbf{m}(\text{Gd})$ (angle geometry as sketched in Fig. 2(a)). Figure 2(b–d) correspond to a first series of images measured with $\phi = 0^\circ$ (Tilt series 1) and Fig. 2(e–g) to a second series of images measured with $\phi \approx 95^\circ$ (Tilt series 2). A clear chevron pattern of alternating out-of-plane stripe domains is observed at normal incidence with period $\Lambda \approx 215\text{nm}$ (see Fig. 2(c, f) at $\vartheta = 0^\circ$). In Tilt series 1 at oblique incidence (sensitive to m_y and m_z), we observe groups of parallel stripes with similar average contrast that is reversed for opposite values of ϑ (see regions labelled as MD1–MD4 in Fig. 2(b, d) at

$\vartheta = \pm 30^\circ$). This indicates that the sample magnetization is broken into a structure of larger magnetic quasi-domains (several μm wide) with similar average in-plane magnetization superimposed on the fast out-of-plane magnetization oscillation of the magnetic stripe pattern. Quasi-domains with a fine-scale internal structure are typical of systems with competing interactions such as magnetostatics and magnetic anisotropy near an arbitrary crystal surface³⁸ or in multivariant ferroelastic materials⁴². These large-scale magnetic quasidomains will be denoted as MD in the following.

However, in Tilt series 2 at oblique incidence (sensitive approximately to m_x and m_z), average in-plane magnetic contrast is weaker than in Tilt series 1. For example, differences in average contrast (measured by subtracting the average signals in each pair of domains) between the pairs MD1/MD4 and MD3/MD2 are reduced by a factor of two in Fig. 2(g) in comparison with Fig. 2(d) indicating that the average in-plane magnetization of these MDs is closer to the y -axis than to the x -axis. This is reasonable since the sample was mounted with the easy anisotropy axis of the $\text{Gd}_x\text{Co}_{100-x}$ layers approximately perpendicular to the rotation axis for Tilt series 1 (i.e., along the y direction).

The 3D configuration of the magnetic moment, $\mathbf{m}(\text{Gd})$, in the multilayer has been obtained from the reconstruction of the MTXM datasets with a vectorial tomography algorithm described in^{32,35}. Since the Co magnetic moment $\mathbf{m}(\text{Co})$ is collinear and antiparallel with $\mathbf{m}(\text{Gd})$ in $\text{Gd}_x\text{Co}_{100-x}$ alloys, its configuration can also be estimated from $\mathbf{m}(\text{Gd})$ vector maps. The physics of the multilayer will be analysed in terms of the magnetic moments of the individual Gd and Co sublattices, i.e., $\mathbf{m}(\text{Gd})$ and $\mathbf{m}(\text{Co})$ and, depending on the magnetic layer, the net magnetization \mathbf{M} will either be parallel or antiparallel to each of them. We will focus on the differences in configuration between the upper and lower regions of the multilayer (i.e., Gd-Co layers), with a more qualitative discussion of the evolution across the thickness.

Out of plane magnetic moment: the role of effective magnetostatic coupling

Analysis of experimental vector tomograms. The vector map of magnetic moments at MD1 obtained from the tomographic reconstruction reveals a complex 3D configuration as shown in Fig. 3. There is a pattern of parallel stripe domains with alternating positive/negative m_z with a period $\Lambda = 215\text{nm}$ both at the top $\text{Gd}_{24}\text{Co}_{76}$ layer (Fig. 3(a)) and at the bottom $\text{Gd}_{12}\text{Co}_{88}$ one (Fig. 3(b)). However, the m_z oscillation at the bottom layer is in antiphase with the oscillation at the top (see e.g., m_z sign along points P_1 to P_3 marked in Fig. 3(a, b) for comparison), and its amplitude is almost three times larger at the bottom than at the top layer.

Figure 3(c) shows a cross section of the magnetic moment vector map taken along a line transverse to the stripe domain pattern (i. e. along the yellow solid arrow in Fig. 3(a, b)). In a large fraction of the sample volume, we observe a typical stripe domain pattern configuration: there is a periodic out-of-plane oscillation of the magnetization with a flux-closed character provided by a closure domain structure³⁸. This shows up in the transverse cross section of Fig. 3(c) as a circulation of the magnetic moment across the thickness in a series of vortices with opposite circulation sense. However, the characteristic stripe configuration does not extend over the whole sample volume. Near the top, we observe a boundary in the magnetic moment vector map where m_z locally reverses its sign. Close to this boundary, m_z contrast becomes weaker indicating that the stripe pattern out-of-plane oscillation is reduced. The evolution of the amplitude of m_z oscillation across the thickness can be quantified

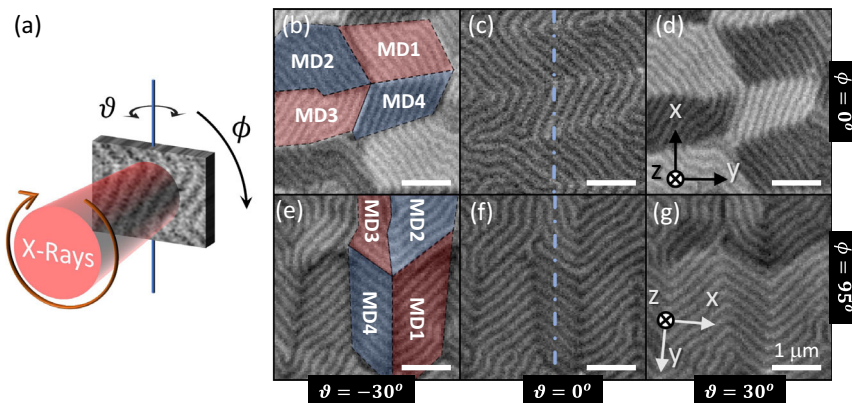


Fig. 2 MTXM images at different angular orientations at Gd $M_{4,5}$ edge. **a** Sketch of X-ray beam/sample geometry at the MISTRAL microscope indicating angles ϑ and ϕ . Tilt series 1 ($\phi = 0^\circ$): **b**) $\vartheta = -30^\circ$; **c**) $\vartheta = 0^\circ$; **d**) $\vartheta = +30^\circ$. Tilt series 2 ($\phi = 95^\circ$): **e**) $\vartheta = -30^\circ$; **f**) $\vartheta = 0^\circ$; **g**) $\vartheta = +30^\circ$. Dashed line indicates rotation axis for each tilt series. Gray scale in MTXM images indicates magnetic contrast, given by the projection of the magnetic moment along the X-ray beam direction (bright/dark contrast corresponds to local magnetic moment parallel/antiparallel to the X-ray beam). Thus, depending on the angle of incidence, images in Tilt series 1 are sensitive to m_y and m_z , whereas images in Tilt series 2 are sensitive to m_z and approximately m_x . Labels and blue/red shades indicate Magnetic quasi-Domains (MD) with different average in-plane magnetization.

by the average angle of oscillation of the stripe pattern at MD1. As sketched in the inset of Fig. 3(d), $\gamma = asin(m_z)$, so that the angular oscillation of the stripe pattern can be determined by the average $\langle |\gamma| \rangle$ within each (x, y, z_i) plane, where z_i indicates the plane position through the sample thickness. Figure 3(d) shows a profile of the angle $\langle |\gamma| \rangle$ vs. z_i at MD1. Near the top of the sample, the amplitude of oscillation is about 20° , it decreases to a minimum of 15° at the m_z reversal boundary and reaches a maximum of 55° at a vertical position 120 nm below this boundary. That is, the minimum $\langle |\gamma| \rangle$ occurs near the GdCo_{TOP}/NdCo interface whereas its maximum is located near the GdCo_{BOTTOM}/NdCo interface, suggesting that the opposite signs of ϵ^{TOP} and ϵ^{BOT} are responsible for the changes in magnetic moment configuration across the multilayer thickness.

Magnetostatic vs. exchange interactions. We will now rationalize the previous finding on the oscillation amplitudes. First, let us consider the central NdCo layer which generates the stripes due to a competition between out-of-plane anisotropy K_{NdCo} (i.e., the uniaxial anisotropy at NdCo with easy axis normal to the film plane) and magnetostatics. Then, there are two energy terms that contribute to imprint the stripe domains into the neighbouring GdCo layers: exchange interaction and magnetostatic coupling (see the sketch in Fig. 3(e)). The exchange E_{ex} between Co moments in each layer ($\mathbf{m}(Co)_{GdCo}$ and $\mathbf{m}(Co)_{NdCo}$) can be written as

$$E_{ex} = -J(Co - Co)\mathbf{m}(Co)_{GdCo} \cdot \mathbf{m}(Co)_{NdCo} \quad (2)$$

and will favour the parallel alignment of $\mathbf{m}(Co)$ at both sides of the interfaces since $J(Co - Co) > 0$.

Next, we consider the magnetostatic energy of the exchange-coupled multilayer³⁸ that, in general, is the sum of two contributions: intralayer energy due to the self-interaction of each magnetic layer and interlayer energy due to the interactions between the layers⁴³. In particular, magnetostatic coupling between GdCo and NdCo layers is given by $E_m = -\frac{1}{2}\mu_0\mathbf{M}(GdCo)\mathbf{H}_d(NdCo)$ ⁴⁴, i.e., it depends on the interaction between $\mathbf{M}(GdCo)$, the net magnetization at the GdCo layer, and $\mathbf{H}_d(NdCo)$, the field created by magnetic charges at the NdCo layer. Here, it can be written as

$$E_m = -\frac{1}{2}\mu_0\epsilon\mathbf{m}(Co)_{GdCo}\mathbf{H}_d(NdCo) \quad (3)$$

where we have explicitly introduced the proportionality factor between $\mathbf{M}(GdCo)$ and $\mathbf{m}(Co)_{GdCo}$. In this way, magnetostatic coupling can be described as an effective field $\epsilon\mathbf{H}_d(NdCo)$ acting on $\mathbf{m}(Co)_{GdCo}$.

At the GdCo_{BOTTOM}/NdCo interface, $\epsilon^{BOT}\mathbf{H}_d(NdCo)$ and $\mathbf{m}(Co)_{NdCo}$ are parallel (since $\epsilon^{BOT} > 0$) and with strong out-of-plane components. Thus, they cooperate to imprint the out-of-plane stripe domain oscillation into the bottom GdCo layer as seen in Fig. 3(e). Below the GdCo_{BOTTOM}/NdCo interface, the circulating $\epsilon^{BOT}\mathbf{H}_d(NdCo)$ will create the characteristic closure domain pattern observed in Fig. 3(c) near the bottom of the multilayer to reduce magnetostatic energy of the sample.

The role of this effective field $\epsilon\mathbf{H}_d(NdCo)$ is qualitatively different at the top GdCo layer. At the GdCo_{TOP}/NdCo interface, $\epsilon^{TOP}\mathbf{H}_d(NdCo)$ is antiparallel to $\mathbf{m}(Co)_{NdCo}$ (since $\epsilon^{TOP} < 0$) so that magnetostatic and exchange couplings compete with each other, as is typical in ferrimagnetic exchange spring walls¹². The exchange coupling should decay faster than the magnetostatic one above the interface so that, at some point, m_z will change the sign under the effect of $\epsilon^{TOP}\mathbf{H}_d(NdCo)$ as observed in Fig. 3(a) and 3(b). The vertical location of this $+m_z/-m_z$ boundary is given by the minimum in $\langle |\gamma| \rangle$ observed in Fig. 3(d).

Thus, the magnetic $+m_z/-m_z$ boundary observed in the magnetic vectorial tomograms in Fig. 3 is the signature of a locally modulated exchange spring wall across the multilayer thickness driven by the magnetostatic coupling with the stripe domain pattern of the NdCo layer. The qualitative differences between the magnetic moment configuration near the top and bottom of the sample give further confirmation of the opposite signs of effective interlayer coupling at both GdCo_{TOP}/NdCo and GdCo_{BOTTOM}/NdCo interfaces in agreement with the multilayer design.

In-plane magnetic moments: uniaxial anisotropy vs. interfacial exchange

Analysis of experimental vector tomograms. Figure 4 shows similar views of the vector tomogram at MD1 as discussed above but now contrast is given by the in-plane component of the magnetic moment m_y in order to analyze the in-plane magnetic configuration. Near the top of the multilayer (Fig. 4(a)), we observe an almost uniform m_y contrast, with a smooth oscillation of the

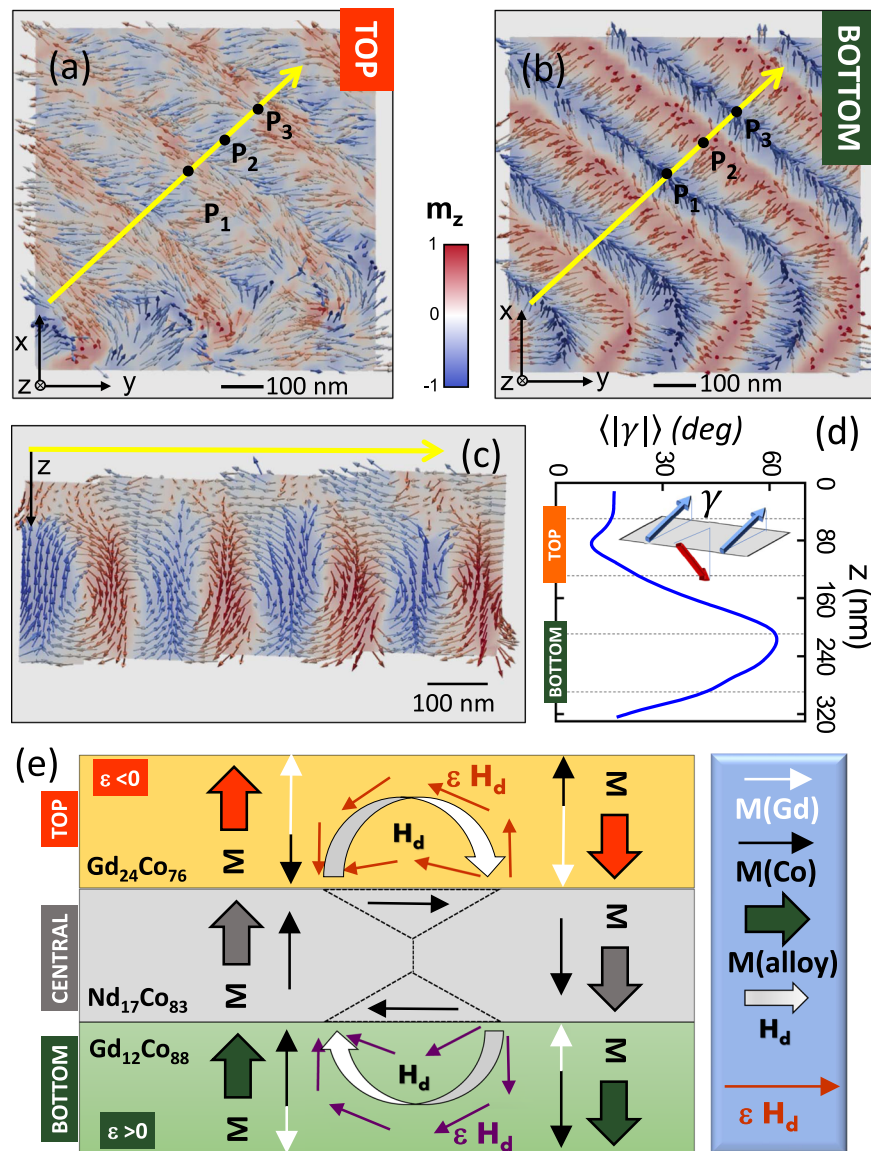


Fig. 3 Vectorial tomographic reconstruction of $m(\text{Gd})$ at MD1 (m_z contrast). **a** View of the $(x, y, 14\text{nm})$ plane (Top Gd-Co layer). **b** View of the $(x, y, 255\text{nm})$ (bottom Gd-Co layer). **c** Cross-section across yellow arrow in **(a)**. Blue/red regions correspond to average up ($+m_z$)/down ($-m_z$) domains. Note the reversed m_z contrast across the sample thickness. **d** Profile of average magnetization oscillation across the thickness (measured as $\langle |\gamma| \rangle$) within each (x, y, z_i) plane. Inset shows a sketch of out-of-plane magnetic moment oscillation within a (x, y, z_0) plane with amplitude γ . Dashed lines indicate nominal boundaries of Top/Bottom Gd-Co layers. **e** Sketch of multilayer configuration and out-of-plane competing interactions.

magnetic moment around an average in-plane orientation. At the bottom of the multilayer (Fig. 4(b)), the in-plane magnetic moment configuration is less homogeneous and a periodic pattern of closure domains is observed. A cross section of the magnetic moment vector map taken along the solid line in Fig. 4(a) reveals again qualitative differences in the Gd magnetic moment configuration across the thickness (see Fig. 4(c)). Above the exchange spring boundary, there is an in-plane magnetic domain with almost uniform m_y contrast. Below this boundary, we find the closure domain pattern made of triangular domains with opposite senses of the in-plane magnetic moment transverse to the stripe pattern (see sketch in Fig. 4(e)). However, there are subtle deviations from the standard symmetric closure domains configuration that usually surrounds the Bloch domain walls between stripe domains^{35,38}. Here, $-m_y$ closure domains are larger than $+m_y$ domains and the cores of closure domain vortices are placed in a zig-zag pattern across

the thickness (see vorticity map in Fig. 4(d), where vorticity is calculated as $|\nabla \times \mathbf{m}|$). This closure domain asymmetry is enhanced near the exchange spring boundary (where the asymmetry in size between $-m_y/+m_y$ domains reaches $\sim 0.2\lambda$) and implies a nonzero in-plane magnetic moment transverse to the stripe domain pattern²⁵.

Asymmetries of the in-plane configuration can be quantified in more detail by histograms of the in-plane moment orientations for different reconstructed planes, as shown in the insets of Fig. 4(a, b). Near the top of the multilayer, we find a relatively narrow distribution of in-plane angles centered at the average angle $\varphi_m^{\text{MD1}} = -75^\circ$ (calculated from the average of the histogram) within an interval $\Delta\varphi = 60^\circ$ (estimated from the FWHM of the histogram). Two maxima are observed in the angular histogram indicating a smooth ripple-like oscillation of the in-plane magnetic moment around φ_m^{MD1} . The aperture β of this oscillation can be estimated from the distance between these

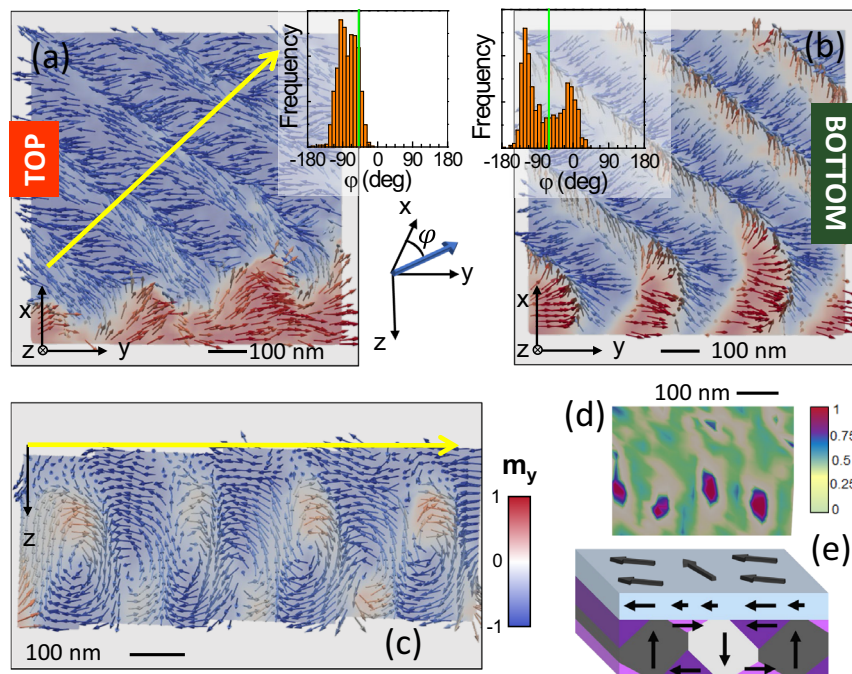


Fig. 4 Vectorial tomographic reconstruction of $m(\text{Gd})$ at MD1 (m_y contrast). **a** View of the $(x, y, 14\text{nm})$ plane (Top Gd-Co layer); **b** View of the $(x, y, 255\text{nm})$ plane (bottom Gd-Co layer); Insets are histograms of in-plane angular orientations respect to the x -axis (φ) within top/bottom layers respectively. Red/blue regions correspond to average in-plane domains with opposite m_y contrast. Vertical line marks stripe domain orientation ($\varphi_{\text{stripe}}^{\text{MD1}} = -50^\circ$). **c** Cross-section across yellow arrow in **(a)**. Note the uniform m_y contrast at top layer and the asymmetric size of opposite closure domains. **d** Detail of the vorticity map at cross section in **(c)**. Note the zig-zag configuration of high vorticity regions corresponding to cores of closure domain vortices. **e** Sketch of domain configuration across the thickness.

two maxima in the angular distribution as $\beta \approx 35^\circ$. Note that the average magnetic moment orientation in MD1 is not aligned with the stripe pattern orientation (marked by a vertical line at $\varphi_{\text{stripe}}^{\text{MD1}} = -50^\circ$ at the inset of Fig. 4(a)). Near the bottom of the multilayer, the angular histogram shows two well-spaced maxima ($\beta = 120^\circ$ and $\Delta\varphi = 150^\circ$) corresponding to opposite in-plane closure domains located at symmetric positions relative to the stripe pattern orientation $\varphi_{\text{stripe}}^{\text{MD1}}$. A certain asymmetry appears between the relative weights of these two maxima in the angular histogram that favours the closure domains nearer to the top layer orientation.

Model of competing interfacial exchange and in-plane anisotropy. Several relevant characteristics of the magnetic configuration of the multilayer can be extracted from the analysis of the vector tomogram: a) closure domains are larger for parallel alignment with the magnetic moment at the top MD1; b) the angular distribution of in-plane magnetic moments at the top MD1 is relatively narrow and not far from the stripe pattern orientation; c) the average in-plane magnetic moment transverse to the stripe pattern is nonzero.

These facts suggest a positive effective interlayer coupling between in-plane moments at the $\text{GdCo}_{\text{TOP}}/\text{NdCo}$ interface dominated by $J(\text{Co}-\text{Co})$ acting on $\mathbf{m}(\text{Co})_{\text{NdCo}}$ and $\mathbf{m}(\text{Co})_{\text{GdCo}}$ with a negligible contribution from magnetostatic coupling. In-plane demagnetization fields are maximum in the plane transverse to the stripe pattern (and are almost negligible in the direction longitudinal to the stripes), therefore their effect would be very small at the observed φ_m^{MD} orientation. Also, the average in-plane moment transverse to the stripes points to a relevant role of in-plane anisotropy not aligned with the stripe domain pattern. In this framework, we propose a simple analytical model to describe the main qualitative features of

the multilayer magnetic configuration based in the balance between the interfacial exchange at $\text{GdCo}_{\text{TOP}}/\text{NdCo}$ and the in-plane uniaxial anisotropy. The geometry of our model is sketched in Fig. 5(a, b): at a certain magnetic quasi-domain MD, the stripe domain pattern in the NdCo_5 layer is oriented at $\varphi_{\text{stripe}}^{\text{MD}}$, determined by magnetic history, while the in-plane anisotropy axis of the top $\text{Gd}_{24}\text{Co}_{76}$ layer, defined by oblique incidence during sample fabrication, is oriented at φ_K . The misorientation between the stripe domains and the easy axis can be defined as $\alpha_K = |\varphi_K - \varphi_{\text{stripe}}^{\text{MD}}|$ taking the shortest angular interval between them.

Now, we assume that this in-plane MD within the top $\text{Gd}_{24}\text{Co}_{76}$ layer is broken up into a periodic pattern of smaller domains of width 0.5Λ , aligned with the underlying closure domain pattern at the top surface of the NdCo layer (see Fig. 5(a)) in order to model the observed ripple-like oscillation. The orientation of the magnetic moment in these two domains relative to the stripe pattern orientation is given by the in-plane angles α_1 and α_2 . The average orientation of the magnetic moment relative to the stripes direction will be $\alpha_m = \frac{\alpha_1 + \alpha_2}{2}$ and the oscillation aperture $\beta = \alpha_1 - \alpha_2$. Then, the anisotropy energy at the top $\text{Gd}_{24}\text{Co}_{76}$ layer in each stripe period Λ can be written as

$$E_K = -\frac{\Lambda}{2} K_{\text{GdCo}} (\cos^2(\alpha_1 - \alpha_K) + \cos^2(\alpha_2 - \alpha_K)) \quad (4)$$

where K_{GdCo} is the in-plane uniaxial anisotropy of the GdCo layer. Equation (4) takes the form

$$E_K = -K_{\text{GdCo}} \Lambda \left(\sin^2 \frac{\beta}{2} + \cos \beta \cos^2(\alpha_m - \alpha_K) \right) \quad (5)$$

in terms of β and α_m . Thus, the effective anisotropy energy acting on the average magnetic moment of MD oriented at α_m decreases as a function of oscillation aperture β by a factor $\cos\beta$.

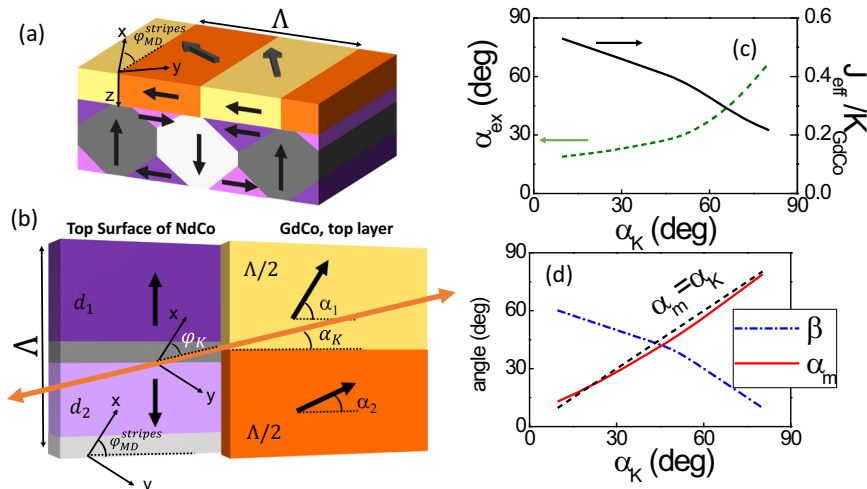


Fig. 5 Model of in-plane interactions. **a** Sketch of cross section of the multilayers with asymmetric closure domains. **b** Sketch of relevant exchange interactions between asymmetric closure domains (width d_1 and d_2) at the top surface of the NdCo layer and quasi domains at GdCo top layer (oriented at α_1 and α_2). Double arrow indicates in-plane easy axis at top GdCo layer oriented at an angle α_K relative to stripe domain pattern. **c** Dependence of effective exchange energy $\frac{J_{\text{eff}}}{K_{\text{GdCo}}}$ (black solid line) and exchange angle α_{ex} (green dashed line) on α_K for $J_{\text{int}}/K_{\text{GdCo}} = 1$ and $d_1 - d_2 = 0.2\Lambda$. **d** Dependence of average magnetization orientation α_m (red solid line) and oscillation aperture β (blue dotted line) on α_K . Dashed black line corresponds to the condition of symmetric oscillation around the easy anisotropy axis.

Now, considering only in-plane components of the magnetic moment, we may write the exchange coupling $E_{\text{ex}}^{\text{ip}}$ at GdCo_{TOP}/NdCo interface as

$$E_{\text{ex}}^{\text{ip}} = -J_{\text{int}} \left(d_1 \cos\left(\frac{\pi}{2} - \alpha_1\right) + d_2 \cos\left(-\frac{\pi}{2} - \alpha_2\right) \right) \quad (6)$$

The first term in Eq. (6) corresponds to the exchange between the closure domain of width d_1 at the top surface of the NdCo layer with the ripple-like domain oriented at α_1 within the top GdCo layer, whereas the second term describes the exchange interaction between the opposite closure domain of width d_2 and the ripple-like domain oriented at α_2 . If α_1 and α_2 are written in terms of the average MD parameters α_m and β , Eq. (6) can be expressed as

$$E_{\text{ex}}^{\text{ip}} = -J_{\text{eff}} \Lambda \cos(\alpha_m - \alpha_{\text{ex}}) \quad (7)$$

with $\tan \alpha_{\text{ex}} = \frac{d_1 - d_2}{\Lambda} \cotan \frac{\beta}{2}$ and $J_{\text{eff}} = J_{\text{int}} \sqrt{\frac{(d_1 - d_2)^2}{\Lambda^2} \cos^2 \frac{\beta}{2} + \sin^2 \frac{\beta}{2}}$. Thus, exchange interactions at the GdCo_{TOP}/NdCo interface take the form of an effective exchange energy that depends on closure domain asymmetry and on the ripple-like oscillation aperture. The sign of the effective exchange angle α_{ex} depends on the closure domain asymmetry $\frac{d_1 - d_2}{\Lambda}$, indicating that $E_{\text{ex}}^{\text{ip}}$ drives the average in-plane $\mathbf{m}(\text{Co})_{\text{GdCo}}$ towards the net in-plane $\mathbf{m}(\text{Co})_{\text{NdCo}}$ of the closure domain structure.

The total energy of the average magnetic moment of the MD is a combination of uniaxial anisotropy and effective exchange

$$E_T = -K_{\text{GdCo}} \Lambda \sin^2 \frac{\beta}{2} - K_{\text{GdCo}} \Lambda \cos \beta \cos^2(\alpha_m - \alpha_K) - J_{\text{eff}} \cos(\alpha_m - \alpha_{\text{ex}}) \quad (8)$$

that must be minimized in terms of α_m and β for each stripe pattern configuration (given by the closure domain asymmetry $\frac{d_1 - d_2}{\Lambda}$ and the misalignment between the easy anisotropy axis and the stripe pattern orientation α_K). In general, uniaxial anisotropy will try to minimize β and make $\alpha_m \approx \alpha_K$, whereas exchange interactions will favour large β values and $\alpha_m \approx 0$. Figure 5(c, d) show the results of E_T minimization for $J_{\text{int}}/K_{\text{GdCo}} = 1$ and $d_1 - d_2 = 0.2\Lambda$, given by the experimental configuration in Fig. 4, as a function of α_K .

The evolution of J_{eff} vs. α_K is a consequence of the lateral averaging of exchange interactions, which fluctuate strongly within each period of the stripe pattern, on the larger length scale of a MD modulated by the ripple-like oscillation around the easy axis. At small α_K , i.e., for stripe domains almost aligned with easy anisotropy axis, minimum energy corresponds to $\alpha_m \approx \alpha_K$ and large $\beta \approx 60^\circ$. This results in relatively large $\frac{J_{\text{eff}}}{K_{\text{GdCo}}}$ and small α_{ex} , so that the ripple-like oscillation is symmetric around the stripe pattern and with a large angular aperture. As α_K increases, we observe slight deviations of α_m from the easy axis orientation and a strong reduction of the oscillation aperture β . Effective exchange J_{eff} decreases and the effective exchange angle α_{ex} approaches the orientation of the easy anisotropy axis. Thus, for large α_K , the magnetic moment at the top GdCo layer would perform a low amplitude ripple-like oscillation around the easy anisotropy axis far away from the stripe domain orientation.

It is interesting to mention that a key feature of this model is that α_K , the misorientation between the in-plane easy axis and the stripe domains, is the relevant parameter that determines the effective coupling between layers and the global configuration of GdCo layer. α_K can be easily varied with the direction of the last saturating field, providing an external knob to adjust the multilayer configuration with the remanent stripe domain orientation.

Global view of in-plane magnetic domains at top GdCo layer.

Figure 6 shows a large view of the magnetic tomogram at the top GdCo layer that includes several in-plane MDs with different signs of average m_y contrast, different stripe orientation and different aperture of the ripple-like oscillations (see Supplementary Note 2 for a detailed view of the fine structure of the magnetization within each quasi-domain). We will use our analytical model to provide a unified picture of these different MDs and approximately determine the orientation of the in-plane easy axis of the multilayer.

MD1 and MD2 are two domains with similar stripe orientation but opposite signs of average m_y contrast, i. e. opposite signs of their average in-plane $\mathbf{m}(\text{Gd})$ orientation. Angular histograms at

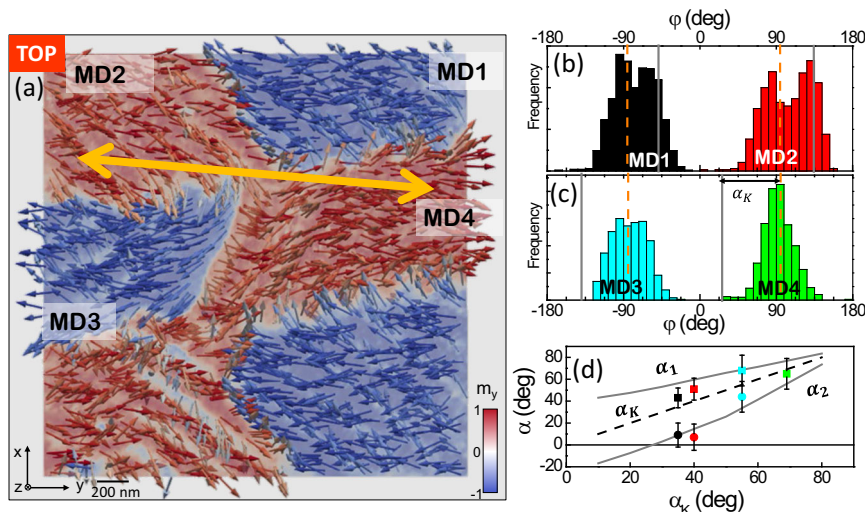


Fig. 6 Statistics of magnetic moment orientation in the quasi domains. **a** Vectorial tomogram reconstruction of $\mathbf{m}(\text{Gd})$ at the $(x, y, 14\text{nm})$ plane (Top Gd-Co layer) with m_y contrast. Red/blue regions correspond to average in-plane domains with opposite m_y contrast. Double arrow indicates the easy anisotropy axis derived from the analytical model. **b, c** Histograms of in-plane angular orientations (ϕ) respect to the x -axis for the different MDs. Vertical solid lines indicate stripe orientation $\phi_{\text{stripe}}^{\text{MD}}$ in each MD region and vertical dashed lines indicate easy axis orientation ϕ_K . **(d)** Ripple-like domain orientation α_1 (squares) and α_2 (circles) vs. α_K . Solid lines are calculated from the analytical model with the same parameters as in Fig. 5. Symbols correspond to experimental α_1 and α_2 obtained from the shortest angular distance between maxima in the histograms and $\phi_{\text{stripe}}^{\text{MD}}$. The parameter α_K in each MD is obtained from the shortest angular distance between $\phi_{\text{stripe}}^{\text{MD}}$ and ϕ_K as indicated in (c). Error bars are one standard deviation from the mean, calculated in the angular range around each maximum in the histograms.

MD1 and MD2 (see Fig. 6(b)) show the same qualitative behavior as in Fig. 4: two clear maxima in the angular distribution with an aperture $\beta \approx 35^\circ - 45^\circ$ and average magnetic moment orientation not too far from the stripe pattern orientation, indicated as vertical continuous lines in Fig. 6(b). Note that for each domain there are two possible values of $\phi_{\text{stripe}}^{\text{MD}}$, separated 180° , and we have selected the closest one to the measured average orientation for each domain, i.e. $\phi_{\text{stripe}}^{\text{MD1}} = -50^\circ$ and $\phi_{\text{stripe}}^{\text{MD2}} = 135^\circ$ (instead of the equivalent $\phi_{\text{stripe}}^{\text{MD2}} = -45^\circ = 135^\circ - 180^\circ$). With this criterion, the misorientation between the average in-plane magnetization and the stripe pattern is $\alpha_m = |\phi_m^{\text{MD}} - \phi_{\text{stripe}}^{\text{MD}}| \approx 25^\circ$, relatively small in both cases, suggesting that α_K is not very large for MD1 and MD2.

Magnetic quasi-domains MD3 and MD4 correspond to the other branch of the zig-zag stripe patterns observed in Fig. 2 with stripe orientation $\phi_{\text{stripe}}^{\text{MD4}} = +26^\circ$ (and the similar $\phi_{\text{stripe}}^{\text{MD3}} = 40^\circ - 180^\circ = -140^\circ$). In this case, the oscillation aperture is smaller and, actually, in MD4 a single maximum is observed in the angular distribution centred at $\phi_m^{\text{MD4}} = 91^\circ$. This reduction in oscillation aperture and the large angular difference between ϕ_m^{MD4} and stripe pattern orientation, suggest that α_K should be the largest at MD4 and that its average in-plane moment should be oriented along the easy anisotropy axis, i.e., $\phi_m^{\text{MD4}} \approx \phi_K$ (and, consequently, $\alpha_m \approx \alpha_K$).

We have tested this hypothesis with a comparison between the experimental ripple-like oscillations observed in the tomogram and α_1 and α_2 values calculated from the analytical model (with the same parameters used in Fig. 5). The experimental α_1 and α_2 of the ripple-like domains have been defined by the positions of the maxima in Fig. 6(b, c) measured as the shortest angular interval from $\phi_{\text{stripe}}^{\text{MD}}$ at each MD. α_K is estimated from the shortest $|\phi_K - \phi_{\text{stripe}}^{\text{MD}}|$ interval as indicated in Fig. 6(c) for each of the four MDs, so that we can make a plot of the experimental $\alpha_{1,2}$ vs. α_K values for each particular ϕ_K as shown in Fig. 6(d). The best

qualitative agreement is found for $\phi_K = 95^\circ$, with most experimental data points lying within the angular interval defined by the theoretical $\alpha_1(\alpha_K)$ and $\alpha_2(\alpha_K)$ trends. It corresponds to the easy axis located at the large double arrow in Fig. 6(a), and at the dashed vertical lines at the histograms in Fig. 6(b, c). In all cases, the average magnetization orientation lies close to the stripe domain orientation, in line with the predictions from the analytical model based on the lateral averaging of exchange interactions within the ripple-like pattern. That is, our multilayer is an experimental realization of an exchange spring system in which effective coupling is not simply determined by material parameters fixed during sample fabrication but, rather, it can be externally adjusted with magnetic history (i.e. with the orientation of the stripe pattern at remanence).

Domain wall between chevron magnetic domains. Finally, let us discuss the magnetic configuration at the corners of the stripe domain chevron pattern (e. g. at the boundary between MD1 and MD4 as sketched in Fig. 7(a)). Here, the stripe pattern rotates by $\Delta\phi_{\text{stripe}}^{\text{MD1-MD4}} = 76^\circ$ whereas the average magnetic moment orientation changes by $\Delta\phi_m^{\text{MD1-MD4}} = 166^\circ$ creating a high angle domain wall between MD1 and MD4. This wall is oriented at $\phi_{\text{DW}} \approx 82^\circ$, i.e. it is almost parallel to the average in-plane magnetic moment at the top GdCo layer of MD1 and MD4 and makes similar angles with the stripe patterns in both chevron MDs so that it is a low energy wall from the magnetostatic point of view.

The domain wall has a complex 3D configuration with a peculiar undulating pattern of period Λ of interleaving $\pm m_y$ regions. Also, the vertical cross section along the domain wall core (Fig. 7(b, c)) presents clear differences from the configuration within each MD (shown in Fig. 4).

First, note that the size of $+m_y/-m_y$ closure domains is similar and closure vortex cores are aligned at a constant

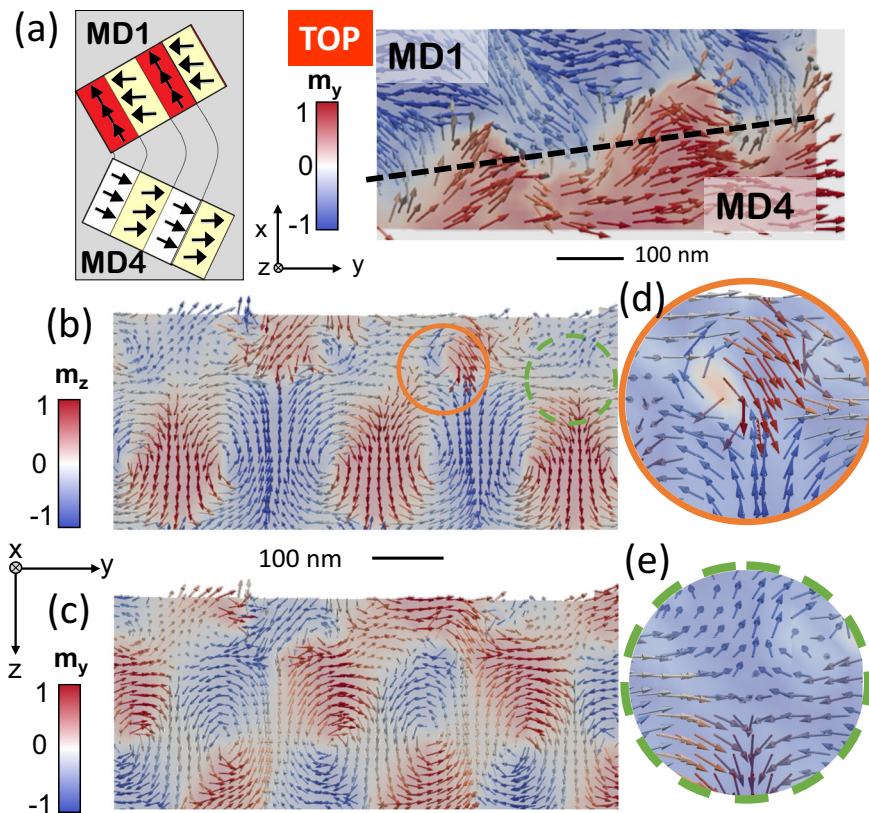


Fig. 7 Tomographic reconstruction of $m(\text{Gd})$ at the domain wall between MD1 and MD4. **a** Sketch of the boundary between MD1 and MD4 at a zig-zag corner of the stripe pattern and zoom view of magnetic tomogram at the $(x, y, 14\text{nm})$ plane (Top Gd-Co layer) with m_y contrast. **(b, c)** Vertical cross-section along domain wall (dashed line in **(a)**) with m_z and m_y contrast, respectively. Note the antiparallel alignment of the magnetic moments at the exchange spring wall across the thickness both in m_z and m_y components and the symmetric configuration of closure domains. **(d, e)** Details of localized vortices (orange solid circle in **(b)**) and antivortices (green dashed circle in **(b)**) at the interface.

z_i position within the multilayer. This can be attributed to the continuous transition between MD1 and MD4. Within each MD, the sign of the average in-plane magnetic component $\langle m_y \rangle = \sin(\varphi_m^{MD})$ is directly related with the sign of $\delta d = d_1 - d_2$, the closure domain asymmetry. Since $\langle m_y \rangle$ and, consequently, δd have opposite signs at MD1 and MD4, δd must become zero at the domain wall, resulting in the same size $+m_y/-m_y$ closure patterns observed in Fig. 7(c).

Second, at the exchange spring wall near the top of the multilayer, there is a sign reversal in both m_y and m_z components (within each MD the reversal takes place only in m_z). This indicates that the dominant coupling term at the $\text{GdCo}_{\text{TOP}}/\text{NdCo}$ interface favours an antiparallel alignment both for in-plane and out-of-plane magnetic moments (within each MD antiparallel coupling dominates only in m_z).

These observations can be attributed to a subtle change in the competition between the relevant energy terms at the domain wall driven by the rotation of the stripe pattern at the corner of the zig-zag: as the stripe pattern turns from $\varphi_{\text{stripe}}^{MD1} = -50^\circ$ to $\varphi_{\text{stripe}}^{MD4} = +26^\circ$ it becomes perpendicular to the in-plane anisotropy easy axis. This fact has two consequences: 1) in-plane anisotropy axis becomes aligned with the closure domain pattern, 2) in-plane components of \mathbf{H}_d are strongest at the orientation favoured by in-plane anisotropy. Thus, in-plane anisotropy enhances the in-plane antiparallel coupling term proportional to the effective field $\varepsilon^{\text{TOP}} \mathbf{H}_d$ resulting in the sign reversal of m_y at the exchange spring wall. The enhancement of in-plane

antiparallel coupling allows the closure domain pattern to emerge at the top GdCo layer and creates the undulating domain wall profile seen in Fig. 7(a).

At the intersection between the exchange spring wall and the closure domain pattern, the $\mathbf{m}(\text{Gd})$ configuration is highly disordered and a high density of vortices and antivortices appears to accommodate these different competing interactions. For example, several antivortices across the thickness are observed at the tip of out-of-plane domains whereas at other locations the system has nucleated closely spaced vortex/antivortex pairs as shown in Fig. 7(d–e)) (see Supplementary Note 3 for a more detailed analysis in terms of emergent fields³⁵ and magnetic vorticity³⁷).

Conclusions

A $\text{Gd}_{12}\text{Co}_{88}/\text{Nd}_{17}\text{Co}_{83}/\text{Gd}_{24}\text{Co}_{76}$ multilayer has been prepared with competing magnetostatic, exchange and anisotropy interactions and its 3D magnetic configuration has been determined from experimental data by X-ray magnetic vector tomography at the Gd $M_{4,5}$ absorption edges.

The general view of the magnetization at MTXM images shows stripe domains with alternating up and down magnetization arranged in a chevron pattern with alternate positive and negative in-plane magnetizations, i.e., in a set of large-scale magnetic quasi-domains with a rich fine scale internal structure.

The vector tomogram reveals a strong out-of-plane magnetization oscillation at the bottom GdCo layer with a closure domain structure across the thickness. It is caused by the cooperation

between ferromagnetic exchange and magnetostatic coupling at the GdCo_{BOTTOM}/NdCo interface that imprints stripe domains into the GdCo layer and, also, by the need to reduce magnetostatic energy at the multilayer/vacuum interface.

The magnetization of the top GdCo layer is mostly in-plane, with a weak out-of-plane oscillation, and medium-sized in-plane MDs that extend over the different sections of the chevron zig-zags. Local exchange springs, characterized by the sign reversal of m_z across the thickness, are observed near the GdCo_{TOP}/NdCo interface as a result of the effective antiparallel magnetostatic coupling between NdCo and top GdCo.

Ripple-like patterns within large-scale magnetic quasi domains are observed at the top GdCo layer, separated by undulating domain walls decorated by magnetic vortices and antivortices across the thickness. They are the result of the subtle balance between effective antiparallel magnetostatic coupling (which is maximum perpendicular to the stripe domains and minimum along them), uniaxial anisotropy defined during the sample fabrication process and interfacial ferromagnetic exchange (isotropic).

In summary, the detailed description of the trilayer magnetization provided by vector magnetic tomography has allowed us to unravel experimentally the complex behavior of the system without a priori assumptions. It is found that the relevant parameters to obtain an adjustable exchange spring are the fine tuning of interlayer coupling by GdCo stoichiometry, defined during sample fabrication, and the orientation of the magnetic stripes relative to in-plane uniaxial anisotropy, adjustable by magnetic history.

Methods

Sample fabrication and magnetic characterization. Gd₁₂Co₈₈/Nd₁₇Co₈₃/Gd₂₄Co₇₆ multilayers to create exchange springs at the top Gd₂₄Co₇₆ layer were grown by sputtering on 50 nm thick Si₃N₄ membranes^{26,45}. In-plane uniaxial anisotropy of top/bottom GdCo layers was defined during sample deposition by the oblique projection of the direction of the atomic beams relative to the sample surface⁴⁶. The easy axis orientations are parallel at top/bottom layers. Saturation magnetization and uniaxial anisotropy at room temperature in each layer have been obtained from Vibrating Sample Magnetometry (VSM) and Transverse MOKE hysteresis loops¹²: $M_S(\text{GdCo})^{\text{BOT}} = 5.1 \times 10^5 \text{ A m}^{-1}$, $K(\text{GdCo})^{\text{BOT}} = 5.1 \times 10^3 \text{ J m}^{-3}$ and $M_S(\text{GdCo})^{\text{TOP}} = 8.94 \times 10^4 \text{ A m}^{-1}$, $K(\text{GdCo})^{\text{TOP}} = 1.34 \times 10^4 \text{ J m}^{-3}$. At the central NdCo₅ layer, typical parameters are $M_S(\text{NdCo}) = 7 \times 10^5 \text{ A m}^{-1}$ and out of plane anisotropy $K_N(\text{NdCo}) \approx 10^5 \text{ J m}^{-3}$ ²⁸, which is an order of magnitude larger than in GdCo layers. Thus, the NdCo₅ layer with its stripe domain pattern will provide the pinned magnetic configuration within the multilayer.

The 80 nm Gd₁₂Co₈₈/80 nm Nd₁₇Co₈₃/80 nm Gd₂₄Co₇₆ multilayer was prepared in a multidomain state after out-of-plane demagnetization allowing the system to explore the complex energy landscape created by the competing interactions and observe it in a single experiment.

MTXM and soft X-ray vector tomography. The sample was mounted in the high precision rotary stage of the full field X-ray transmission microscope at the MISRAL beamline of ALBA Synchrotron³⁵. One hundred nm gold nanoparticles dispersed on its surface serve as fiducials for accurate projection alignment to a common rotation axis prior to the tomography reconstruction. The sample was illuminated with circularly polarized X-rays with fixed polarization in order to exploit magnetic contrast from X-ray circular dichroism⁴⁷ at the Gd M absorption edges, Gd M₄ (1221.9 eV) and Gd M₅ (1189.6 eV). The sample was rotated around an axis parallel to the sample surface and perpendicular to the horizontal X ray beam, in order to acquire a tilt series of images, i.e., a set of closely spaced MTXM images at 2° intervals in the angular range $\vartheta = \pm 26^\circ$ and at 1° intervals in the angular ranges $[-55^\circ, -26^\circ]$ and $[26^\circ, 55^\circ]$ (see sketch in Fig. 2(a)), $\vartheta = 0^\circ$ when the multilayer normal is parallel to the X ray direction). Tomographic reconstruction of the magnetization vector requires two orthogonal tilt series^{32,33}. Thus, the sample was manually rotated in-plane by an angle $\phi \approx 90^\circ$ and a second tilt series was acquired. Fine alignment of the two tilt series together was also performed as a part of the tomographic reconstruction process with the aid of the gold fiducials³⁵. The actual in-plane angle between the two-tilt series was measured as $\phi \approx 95^\circ$. At each (ϑ, ϕ) orientation, 2D transmitted images were sequentially acquired at the Gd M₄ and Gd M₅ absorption edges since they present opposite signs of the X-ray magnetic circular dichroic factor. Then, either charge (TXM) or magnetic (MTXM) contrast images were obtained by the addition/subtraction of the logarithm of individual transmittance images at Gd M₄ and M₅ edges with a proper normalization to minimize magnetic contrast in the charge images^{35,48}. In general,

magnetic contrast is given by the projection of the magnetic moment along the X-ray beam direction⁴⁷. Normal incidence images are only sensitive to the out-of-plane component of the magnetic moment m_z , whereas tilted incidence images also provide information of the in-plane component of the magnetic moment perpendicular to the rotation axis. Thus, images in Tilt series 1 are sensitive to m_y and m_z , whereas images in Tilt series 2 are sensitive to m_x and approximately m_z .

We can obtain the 3D magnetic moment configuration in the multilayer from the reconstruction of the MTXM datasets in Tilt series 1 and 2 with a vector tomography algorithm^{26,35}. The total reconstructed volume is $2700 \times 2700 \times 2025 \text{ nm}^3$ (with a total of $200 \times 200 \times 150$ voxels and pixel size 13.5 nm), which is much larger than the multilayer thickness. The tomography algorithm properly locates, without any a priori assumptions, the magnetic signal from the multilayer just below the plane defined by the gold fiducials that were placed on the sample surface (see details at Supplementary Note 1). The result is a 3D vector map of the magnetic moments of Gd, $\mathbf{m}(\text{Gd})$, convoluted with the lateral resolution function of the microscope ($\sim 30 \text{ nm}$) and the axial resolution of the measurement. The latter has been estimated to be $\sim 65 \text{ nm}$ (see Supplementary Note 1 for details) which is comparable with individual layer thickness³⁵ and slightly larger than the spatial resolution reported in experiments of magnetic laminography of microdiscs of the order of 50 nm³⁴. An important methodological issue that has to be clear is the following: as we do not impose any a priori condition (i.e., we do not set $m = 0$ at the NdCo central layer), our tomographic reconstruction generates a continuous field of magnetic moments that, due to the finite axial resolution is nonzero in the central layer in spite of not having Gd atoms. This continuity mimics the effect of exchange coupling between layers³⁵. Here, we have focused on the differences in configuration between the upper and lower regions of the multilayer (i.e., GdCo layers), with a more qualitative discussion of the evolution across the thickness.

Data availability

The datasets generated during the current study are available from the corresponding authors on reasonable request.

Received: 8 September 2021; Accepted: 21 December 2021;

Published online: 18 January 2022

References

- Mandru, Andrada-Oana et al. Coexistence of distinct skyrmion phases observed in hybrid ferromagnetic/ferrimagnetic multilayers. *Nat. Commun.* **11**, 6365 (2020).
- Yu, Dobin, A. & Richter, H. J. Domain wall assisted magnetic recording. *J. Appl. Phys.* **101**, 09K108 (2007).
- Beens, M., Lalieu, M. L. M., Deenen, A. J. M., Duine, R. A. & Koopman, B. Comparing all-optical switching in synthetic-ferrimagnetic multilayers and alloys. *Phys. Rev. B* **100**, 220409(R) (2019).
- Bläsing, R. et al. Exchange coupling torque in ferrimagnetic Co/Gd bilayer maximized near angular momentum compensation temperature. *Nat. Commun.* **9**, 4984 (2018).
- Divinskiy, B. et al. Effects of Spin-Orbit Torque on the Ferromagnetic and Exchange Spin-Wave Modes in Ferrimagnetic Co-Gd Alloy. *Phys. Rev. Appl.* **14**, 044016 (2020).
- Brandão, J., Dugato, D. A., Puydinger dos Santos, M. V. & Cezar, J. C. Evolution of Zero-Field Ferrimagnetic Domains and Skyrmions in Exchange-Coupled Pt/CoGd/Pt Confined Nanostructures: Implications for Antiferromagnetic Devices. *ACS Appl. Nano Mater.* **2**, 7532 (2019).
- Caretta, L. et al. Fast current-driven domain walls and small skyrmions in a compensated ferrimagnet. *Nat. Nanotech.* **13**, 1154 (2018).
- Woo, S. et al. Current-driven dynamics and inhibition of the skyrmion Hall effect of ferrimagnetic skyrmions in GdFeCo films. *Nat. Commun.* **9**, 959 (2018).
- Kim, Kab-Jin et al. Fast domain wall motion in the vicinity of the angular momentum compensation temperature of ferrimagnets. *Nat. Mater.* **16**, 1187 (2017).
- Tadout, M. et al. Engineered Gd-Co based multilayer stack to enhanced magneto-caloric effect and relative cooling power. *J. Appl. Phys.* **123**, 053902 (2018).
- Bill, A. & Braun, H. B. Magnetic properties of exchange springs. *J. Magn. Magn. Mat.* **272–276**, 1266–1267 (2004).
- Blanco-Roldán, C. et al. Tuning interfacial domain walls in GdCo/Gd/GdCo' spring magnets. *Phys. Rev. B* **92**, 224433 (2015).
- Magnus, F. et al. Long-range magnetic interactions and proximity effects in an amorphous exchange-spring magnet. *Nat. Commun.* **7**, 11931 (2016).
- Hebler, B., Reinhardt, P., Katona, G. L., Hellwig, O. & Albrecht, M. Double exchange bias in ferrimagnetic heterostructures. *Phys. Rev. B* **95**, 104410 (2017).

15. Quesada, A. et al. Exchange-spring behavior below the exchange length in hard-soft bilayers in multidomain configurations. *Phys. Rev. B* **98**, 214435 (2018).
16. Watson, S. M. et al. Interfacial magnetic domain wall formation in perpendicular-anisotropy, exchange-spring films. *Appl. Phys. Lett.* **92**, 202507 (2008).
17. Lee, T. et al. Strain-Modulated Exchange-Spring Magnetic Behavior in Amorphous Tb-Fe Thin Films. *Phys. Rev. Appl.* **8**, 024024 (2017).
18. Thórarinsdóttir, K. A., Hase, T., Hjörvarsson, B. & Magnus, F. Amorphous exchange-spring magnets with crossed perpendicular and in-plane anisotropies. *Phys. Rev. B* **103**, 014440 (2021).
19. Wang, K. et al. Direct observation of magnetic exchange-spring development in epitaxial DyFe₂/YFe₂ superlattices by magneto-optical Kerr effect. *Funct. Mat. Lett.* **8**, 1550053 (2015).
20. Liu, Y. et al. Magnetic structure in Fe/Sm-Co exchange spring bilayers with intermixed interfaces. *Phys. Rev. B* **83**, 174418 (2011).
21. Fullerton, E. E., Jiang, J. S. & Bader, S. D. Hard/soft magnetic heterostructures: model exchange-spring magnets. *J. Magn. Magn. Mat.* **200**, 392 (1999).
22. Heigl, M. et al. Microscopic Origin of Magnetization Reversal in Nanoscale Exchange-Coupled Ferri/Ferromagnetic Bilayers: Implications for High Energy Density Permanent Magnets and Spintronic Devices, *ACS Appl. Nano Mater.* **3**, 9218–9225 (2020).
23. McCord, J. Progress in magnetic domain observation by advanced magneto-optical microscopy. *J. Phys. D: Appl. Phys.* **48**, 333001 (2015).
24. Beutier, G. et al. Characterization of FePd bilayers and trilayers using soft x-ray resonant magnetic scattering and micromagnetic modelling. *Phys. Rev. B* **71**, 184436 (2005).
25. Fin, S. et al. In-plane rotation of magnetic stripe domains in Fe_{1-x}Ga_x thin films. *Phys. Rev. B* **92**, 224411 (2015).
26. Hierro-Rodríguez, A. et al. Deterministic propagation of vortex-antivortex pairs in magnetic trilayers. *Appl. Phys. Lett.* **110**, 262402 (2017).
27. Blanco-Roldán, C. et al. Nanoscale imaging of buried topological defects with quantitative X-ray magnetic microscopy. *Nat. Commun.* **6**, 8196 (2015).
28. Quiros, C. et al. Cycloidal Domains in the Magnetization Reversal Process of Ni₈₀Fe₂₀/Nd₁₆Co₈₄/Gd₁₂Co₈₈ Trilayers. *Phys. Rev. Appl.* **10**, 014008 (2018).
29. Wohlhüter, P. et al. Nanoscale switch for vortex polarization mediated by Bloch core formation in magnetic hybrid systems. *Nat. Commun.* **6**, 7836 (2015).
30. Donnelly, C. et al. Three-dimensional magnetization structures revealed with X-ray vector nanotomography. *Nature* **547**, 328–331 (2017).
31. Witte, K. et al. From 2D STXM to 3D Imaging: Soft X-ray Laminography of Thin Specimens. *Nano Lett.* **20**, 1305–1314 (2020).
32. Hierro-Rodríguez, A. et al. 3D reconstruction of magnetization from dichroic soft X-ray transmission tomography. *J. Synchrotron Rad.* **25**, 1144–1152 (2018).
33. Donnelly, C. et al. Tomographic reconstruction of a three-dimensional magnetization vector field. *N. J. Phys.* **20**, 083009 (2018).
34. Donnelly, C. et al. Time-resolved imaging of three-dimensional nanoscale magnetization dynamics. *Nat. Nanotechnol.* **15**, 356–360 (2020).
35. Hierro-Rodríguez, A. et al. Revealing 3D magnetization of thin films with soft X-ray tomography: magnetic singularities and topological charges. *Nat. Commun.* **11**, 6382 (2020).
36. E. Josten et al., Curvature-mediated spin textures in magnetic multi-layered nanotubes, *arXiv:2103.13310v1* (2021).
37. Donnelly, C. et al. Experimental observation of vortex rings in a bulk magnet. *Nat. Phys.* **17**, 316–321 (2021).
38. A. Hubert and R. Schafer. *Magnetic Domains: The Analysis of Magnetic Microstructures* (Springer-Verlag, Berlin, 1998)
39. Fujiwara, H., Sugita, Y. & Saito, N. Mechanism of rotatable anisotropy in thin magnetic films of Ni, Fe, and Ni-Fe. *Appl. Phys. Lett.* **4**, 199 (1964).
40. Hierro-Rodríguez, A. et al. Controlled nucleation of topological defects in the stripe domain patterns of Lateral multilayers with Perpendicular Magnetic Anisotropy: competition between magnetostatic, exchange and misfit interactions. *Phys. Rev. B* **88**, 174411 (2013).
41. Dehesa-Martínez, C. et al. Magneto-optical transverse Kerr effect in multilayers. *Phys. Rev. B* **64**, 024417 (2001).
42. Perevertov, O., Heczko, O. & Schäfer, R. Direct observation of magnetic domains by Kerr microscopy in a Ni-Mn-Ga magnetic shape-memory alloy. *Phys. Rev. B* **95**, 144431 (2017).
43. Janicka, K., Burton, J. D. & Tsymbal, E. Y. Effects of magnetostatic coupling on stripe domain structures in magnetic multilayers with perpendicular anisotropy. *J. Appl. Phys.* **101**, 113921 (2007).
44. H. Kronmüller. in *Handbook of Magnetism and Advanced Magnetic Materials* (eds H. Kronmüller, S. Parkin, J. E. Miltat and M. R. Scheinfein), General Micromagnetic Theory and Applications, Wiley online (2007).
45. Hermosa, J. et al. Magnetic textures and singularities in ferri/ferromagnetic multilayers. *J. Magn. Magn. Mater.* **539**, 168384 (2021).
46. Quirós, C. et al. Asymmetric grazing incidence small angle x-ray scattering and anisotropic domain wall motion in obliquely grown nanocrystalline Co films. *Nanotechnology* **25**, 335704 (2014).
47. J. Stöhr and H. C. Siegmann. *Magnetism. From Fundamentals to Nanoscale Dynamics* (Springer, 2006).
48. Fischer, P. et al. Imaging of magnetic domains by transmission x-ray microscopy. *J. Phys. D: Appl. Phys.* **31**, 649–655 (1998).

Acknowledgements

Alba light source is funded by the Ministry of Research and Innovation of Spain, by the Generalitat de Catalunya and by European FEDER funds. This project has been supported by Spanish MICINN under grant PID2019-104604RB/AEI/10.13039/501100011033.

Author contributions

C.Q., J.I.M., M.V. and S.F. designed and planned the experiments, J.H.-M., C.Q. and J.I.M. prepared the samples. J.H.-M., A.H.-R., C.Q., A.S., S.R., E.P. and S.F. carried out the synchrotron experiment. J.H.-M. and A.H.-R. performed the tomographic reconstructions. J.H.-M., A.H.-R., L.M.A.P., J.I.M., C.Q., M.V. and S.F. analyzed the data. All the authors participated in the interpretation and discussion of the results. A.H.-R., M.V. and S.F. wrote the article.

Competing interests

The authors declare no competing interests.

Additional information

Supplementary information The online version contains supplementary material available at <https://doi.org/10.1038/s42005-021-00800-3>.

Correspondence and requests for materials should be addressed to Aurelio Hierro-Rodríguez, María. Vélez or Salvador Ferrer.

Peer review information *Communications Physics* thanks Rudolf Schaefer and the other, anonymous, reviewer(s) for their contribution to the peer review of this work.

Reprints and permission information is available at <http://www.nature.com/reprints>

Publisher's note Springer Nature remains neutral with regard to jurisdictional claims in published maps and institutional affiliations.



Open Access This article is licensed under a Creative Commons Attribution 4.0 International License, which permits use, sharing, adaptation, distribution and reproduction in any medium or format, as long as you give appropriate credit to the original author(s) and the source, provide a link to the Creative Commons license, and indicate if changes were made. The images or other third party material in this article are included in the article's Creative Commons license, unless indicated otherwise in a credit line to the material. If material is not included in the article's Creative Commons license and your intended use is not permitted by statutory regulation or exceeds the permitted use, you will need to obtain permission directly from the copyright holder. To view a copy of this license, visit <http://creativecommons.org/licenses/by/4.0/>.

© The Author(s) 2022